Estimation of transport at open boundaries with an ensemble Kalman filter in a coastal ocean model

Antoni Jordi[1] and Dong-Ping Wang[2]

[1] IMEDEA (UIB-CSIC), Institut Mediterrani d'Estudis Avançats, Miquel Marquès 21, 07190 Esporles, Spain.

[2] School of Marine and Atmospheric Sciences, Stony Brook University, Stony Brook, NY 11794, USA.

Corresponding author: A. Jordi (toni@imedea.uib-csic.es). IMEDEA (UIB-CSIC), Institut Mediterrani d'Estudis Avançats, Miquel Marqués 21, 07190 Esporles, Illes Balears, Spain. Phone: +34971611910. Fax: +34971611761

Abstract

The performance of the ensemble adjustment Kalman filter (EAKF) to estimating volume transports at open boundaries was investigated for a coastal ocean model of the Palma Bay, Mallorca Island, Mediterranean Sea. The circulation in the Palma Bay is mainly driven by the propagation around Mallorca of remotely wind-generated island trapped waves (ITWs) and by a local wind response. Thus, for a model of the bay proper only, the large-scale ITWs must be incorporated into the open ocean boundary conditions. To take into account the effect of ITWs, an EAKF was used to assimilate the moored Acoustic Doppler Current Profiler (ADCP) velocity time series collected in the inner part of the Bay through a simultaneous state and parameter estimation. In this approach, flows at open boundaries were included in the model state as time-dependent parameters and were updated in each assimilation step. The simulation was validated with moored ADCP data as well as with independent towed ADCP spatial velocity survey data. The new results are markedly improved over the model experiments with no state and/or parameter estimation. In particular, simulation using the estimated values at the open boundaries outperforms simulation with 'a priori' prescribed values at boundaries. The error reduction is about 45% when ITWs dominate the circulation. Our results present a promising approach in dealing with the open boundary conditions in a coastal ocean model.

Keywords: Boundary conditions; Kalman filters; Shelf dynamics; Modeling; Mediterranean Sea.

1. Introduction

The choice of boundary conditions at the open boundaries is perhaps the most challenging problem in coastal (limited-area) ocean modeling. The ocean is a dynamic system affected by a wide range of processes interacting in multiple spatial and temporal scales. Modeling the global ocean with a grid capable of resolving the full range of processes is not feasible due to limitations in computer resources. Boundary conditions are thus used to connect a coastal ocean model domain to the rest of the global ocean. The fluid should flow unrestricted at open boundaries in and out of the model domain (Chapman, 1985; Marchesiello et al., 2001). Waves, water masses and other motions generated within the model domain should cross the open boundaries without spurious reflections that influence the model solution. At the same time, processes generated outside the model domain should correctly influence the flows in the model domain when they propagate inward.

Different methods are available for determining the open boundary conditions. Several methods determine the boundary conditions from the model solution in the neighborhood of open boundaries (e.g., Greatbatch and Otterson, 1991; Marsaleix et al., 2006; Palma and Matano, 1998, 2000). This type of boundary conditions has been successfully tested, but it does not provide information into the model domain from the rest of the global ocean. Nesting coastal ocean models into large scale models is one strategy to deal with this issue (Cailleau et al., 2008). The large scale model prescribes the flow to the regional model via the boundary conditions, while the coastal model may (two-way nesting) or may not (one-way nesting) influence the large scale model solution. The performance of various nesting techniques in ocean models has been evaluated in a number of numerical studies (e.g., Barth et al., 2005; Debreu and Blayo, 2008; Oddo and Pinardi, 2008). A potential drawback is that the large scale model might not be as accurate compared to the coastal model due to larger errors in the forcing conditions, spatial resolution, etc.

An alternative approach is the use of available observations through data assimilation to estimate the open boundary conditions (Chu et al., 1997; Jan et al., 2004; Jones and Davies, 2003). The advantage of this approach is in providing information on the open boundary conditions from observations within the model domain rather than using only information from a large scale model. Although nesting models could also include data assimilation in the coastal or both models (Barth et al., 2007; Haley and Lermusiaux,

2010; Haley et al., 2009), we focus here on studies with a single model domain. A common data assimilation approach is the four-dimensional (4D) variational analysis that corrects the model solution and boundary conditions in a dynamically consistent way using the available observations through the use of the model adjoint. However, the implementation of variational techniques could be computationally demanding, especially with high resolution models (Taillandier et al., 2004). To overcome this problem, one often seeks reduced-ranks approximations where the local ocean dynamics is approximated by the linearized model equations (Edwards et al., 2004; Shulman et al., 1999). Nevertheless, the variational analysis has been successfully demonstrated for estimation of external forcing and open boundaries in a coastal application (San Diego Bay, U.S.A.) based on the MITgcm and its adjoint (Hoteit et al., 2009).

The ensemble Kalman filter (EnKF) originally introduced by Evensen (1994) is another class of 4D data assimilation method that is widely used in ocean models. In this approach, an ensemble of model states is integrated forward in time according to the model dynamics to predict error statistics needed for the assimilation. In the Mediterranean Sea, ensemble techniques have been utilized in high-resolution regional ocean models for the determination of model uncertainty and major error sources, including boundary conditions (Auclair et al., 2003; Rixen et al., 2009). Realistic EnKF studies have been carried out in the Mediterranean using the Singular Evolutive Extended Kalman (SEEK) filter to reduce the computational burden (Korres et al., 2007; Korres et al., 2009).

The EnKF also can be used to estimate the open boundary conditions through the state-parameter augmentation approach, by simultaneously estimating the model state vector as well as the optimal boundary condition values (Jazwinski, 1970; Lermusiaux et al., 2006). This concept follows the parameter estimation approach (in our case, the boundary conditions are the parameters) in a data assimilation environment, which has gained an increasing interest in the atmospheric and oceanic numerical modeling community (Evensen, 2009; Lermusiaux and Robinson, 1999). Simultaneous state and parameter estimation with the EnKF has produced encouraging results. Lermusiaux (1999), for example, combined boundary conditions and forcing with standard prognostic variables in an augmented state vector continuously updated through assimilation of observed temperature and salinity profiles with an EnKF method in simulation of the mesoscale variability in the Strait of Sicily (Mediterranean Sea). Also,

Cossarini et al. (2009) estimated the boundary forcing and other physical and biological parameters in a coupled physical-biogeochemical model of the Venice Lagoon.

In this study, we explored the application of the EnKF to the estimation of open boundary conditions in a model of the Palma Bay (Mallorca Island, western Mediterranean Sea, Fig. 1). Jordi et al. (2009b, 2011) have examined the circulation around Mallorca and in the Palma Bay. They found that the circulation is mainly driven by two wind forced mechanisms: remotely generated island trapped waves (ITWs) and local wind-induced response. The ITWs are a special case of coastal trapped waves with an integer number of wavelengths, or continuous phase, around the island (Brink, 1999). ITWs propagate around Mallorca Island at periods of 60 and 24 h and induce different current regimes in the Palma Bay depending on their intensity: weak ITWs induce currents flowing parallel to the coast and strong ITWs form eddies due to flow separation at the capes. Other forcing mechanisms, such as tides and horizontal gradients, do not create significant currents (< 3 cm s^{-1}) in this region. In addition, the circulation is largely uncoupled from the open ocean, although it is eventually subjected to the influence of changes in water mass composition (Jordi et al., 2009a). There are no rivers or permanent freshwater discharges in the Bay and around Mallorca Island.

The coastal ocean model is chosen such that it covers only the Palma Bay. The objective is to include the large-scale circulation induced by the ITWs in the model as open boundary conditions. An EnKF method, the ensemble adjustment Kalman filter (EAKF) (Anderson, 2001), is used to estimate the open boundary conditions through the state augmentation approach. We assume the uncertainty of boundary conditions and treat them as new state variables (parameters) within the numerical model, i.e. as a part of the unknown model states.

2. Material and methods

2.1 Numerical model

The model used in this study is the Princeton Ocean Model (POM), a free-surface ocean general circulation model (Mellor, 1993). The model solves the primitive equations on a horizontal Arakawa C grid and a vertical sigma-level grid under the hydrostatic and Boussinesq assumptions. The numerical scheme is leapfrog in time and centered in space. It also uses mode-split in the vertical. Horizontal mixing is parameterized

according to the Smagorinsky diffusion scheme and vertical mixing coefficients are calculated with a level 2.5 Mellor–Yamada turbulence closure scheme. The bottom friction followed the quadratic law with the drag coefficient set at 0.0025. The model domain was restricted to the Palma Bay (Fig. 1). Therefore, the generation and propagation of the ITWs around Mallorca could not be reproduced by the model. The horizontal resolution was 200 m with 130 × 130 grid points, while there were 31 vertical sigma-levels. Time steps were 2 s for the external mode and 60 s for the internal mode. The model ran from 25 June and 27 October 2009 when complete data sets were available (see below). We used a parallel version of POM (Jordi and Wang, 2012).

As currents in the Palma Bay are mainly driven by wind, the model was forced only by wind and no other forcing such as heat or water fluxes and tides was applied, although temperature and salinity inflows were allowed at open boundaries (see below). Surface wind fields were provided by the Spanish Meteorological Service (AEMET) at 3 h intervals and at a resolution of 0.05º × 0.05º from an operational forecast system based on High Resolution Limited Area Model (HIRLAM). The model was initialized from a state of rest and the initial fields of temperature and salinity were horizontally uniform based on summer climatology with a pycnocline at 25–30 m depth (Fig. 2), similar to the hydrographic profiles obtained in the area (Jordi et al., 2011).

At the open boundaries, we used a combination of transports estimated with the EAKF (see below) along with radiation condition which effectively allows interior disturbances to pass through the lateral boundary

$$u = u_{est} \pm \sqrt{\frac{g}{H}}\eta \qquad (1)$$

where u is the depth-averaged (2D) velocity normal to the boundary, g is gravity, H is depth at the open boundary, η is free surface elevation at the open boundary, the subscript *est* denotes the estimated flow with the EAKF, and the +/- sign refers to the western/eastern (or southern/northern) boundary of the model. For the baroclinic velocities, an Orlanski radiation condition was first used. Then, the 3D structure of currents normal to the boundary was adjusted so that their vertical integrals are equal to the 2D velocity. For temperature and salinity, values at the open boundary were updated using one-sided difference scheme whenever the normal velocity is directed outwards from the model domain. In cases of inflow through the open boundary, temperature and salinity were set equal to the initial temperature and salinity.

177

178 *2.2 Data Assimilation Method*

179 The EAKF used here was based on that developed by Anderson (2001). This algorithm
180 processes each scalar observation sequentially, so that the operation of the EAKF can be
181 accomplished by describing only the impact of a single scalar observation on a single
182 model state vector (Anderson, 2003). First, an ensemble of *N* model state vectors was
183 integrated forward from the time of the previous observation to the time of the next
184 available observation. Using the notation of Ide et al. (1997), forecast (or prior)
185 estimates for this observation ($\mathbf{y}^{\mathrm{f}}$) were computed by applying the observation operator
186 H to each forecast ensemble member of the single model state ($\mathbf{x}^{\mathrm{f}}$). Both $\mathbf{x}^{\mathrm{f}}$ and $\mathbf{y}^{\mathrm{f}}$ are
187 vectors of N elements

188 $$\mathbf{y}^{\mathrm{f}} = H\mathbf{x}^{\mathrm{f}} \tag{2}$$

189 Given the scalar observed value $\mathbf{y}^{\mathrm{o}}$ with observational error covariance $\mathbf{R}$, the Bayes'
190 theorem yielded the analysis (posterior) ensemble estimate for $\mathbf{y}$

191 $$\mathbf{y}^{\mathrm{a}} = \sqrt{\frac{\mathbf{P}^{\mathrm{a}}}{\mathbf{P}^{\mathrm{f}}}}\left(\mathbf{y}^{\mathrm{f}} - \overline{\mathbf{y}^{\mathrm{f}}}\right) + \overline{\mathbf{y}^{\mathrm{a}}} \tag{3}$$

192 where $\overline{\mathbf{y}^{\mathrm{f}}}$ and $\mathbf{P}^{\mathrm{f}}$ are the forecast ensemble mean and covariance, respectively. The
193 analysis ensemble mean and covariance, $\overline{\mathbf{y}^{\mathrm{a}}}$ and $\mathbf{P}^{\mathrm{a}}$, are

194 $$\overline{\mathbf{y}^{\mathrm{a}}} = \mathbf{P}^{\mathrm{a}}\left(\frac{\overline{\mathbf{y}^{\mathrm{f}}}}{\mathbf{P}^{\mathrm{f}}} + \frac{\mathbf{y}^{\mathrm{o}}}{\mathbf{R}}\right) \tag{4}$$

195 $$\mathbf{P}^{\mathrm{a}} = \left[\left(\mathbf{P}^{\mathrm{f}}\right)^{-1} + \left(\mathbf{R}\right)^{-1}\right]^{-1} \tag{5}$$

196 Finally each ensemble member for the state variable was updated by doing a linear
197 regression of the observation space increments ($\mathbf{y}^{\mathrm{a}}$ □ $\mathbf{y}^{\mathrm{f}}$) onto the state vector component
198 using the forecast joint ensemble sample statistics

199 $$\mathbf{x}^{\mathrm{a}} = \mathbf{x}^{\mathrm{f}} + \frac{\mathrm{P}_{\mathbf{x},\mathbf{y}}}{\mathbf{P}^{\mathrm{f}}}\left(\mathbf{y}^{\mathrm{a}} - \mathbf{y}^{\mathrm{f}}\right) \tag{6}$$

200 where $\mathbf{P}_{\mathbf{x},\mathbf{y}}$ is the forecast sample covariance between the model states $\mathbf{x}^{\mathrm{f}}$ and $\mathbf{y}^{\mathrm{f}}$,
201 determined directly from the ensemble. This algorithm was sequentially applied for
202 each model state variable and each scalar observation. To increase the computational

efficiency, we used a parallel implementation of the EAKF algorithm following Anderson and Collins (2007).

In the parameter estimation approach of the EAKF, the augmented state vector, the regular state variables (sea level, temperature, salinity, and horizontal velocity components) plus parameters, is updated through Eq. 5 using the covariance between the predicted data and the regular state variables or parameters. In our case, parameters were volume transports at open boundaries (specifically, depth-averaged velocities normal to the corresponding boundaries). To avoid spurious large correlation between greatly separated grid points, we localized the impact of the observations over the regular model state space by multiplying the Kalman gain with a covariance cut-off function from Gapari and Cohn (1999). The selected cut-off distance was 2000 m. Unlike regular state variables, parameters to be estimated were not affected by this cut-off distance.

The EAKF requires an ensemble of model states for initialization. A 32 ensemble members were generated by setting randomly the transport at open boundaries at model initialization. Three sets (each for one open boundary in the model) of 32 random values drawn from a normal distribution with zero mean and a standard deviation of 10 cm s^{-1} were generated (currents at boundaries ranged approximately from -20 to 20 cm s^{-1}). These boundary values were updated every 3 h simultaneously with regular state variables when new observations were assimilated but remained constant during model integration. In addition, the variances of boundary values after each assimilation step were multiplied by a value so that posterior and prior variances were equal following the inflation technique of Anderson and Anderson (1999). This step is required in parameter estimation. The variance of both model variables and parameters is reduced at assimilation steps, but parameters remain constant between assimilation steps unlike model variables. Therefore, parameters variance decreases progressively and may lead to filter divergence (i.e. observations have progressively smaller impact), especially if true parameter values vary in time (Aksoy et al., 2006), as in our study.

2.3 Data

Assimilated observational data consisted of velocity time series collected in the Palma Bay. The main features of observed currents are described in detail by Jordi et al.

(2011). In this study we concentrated on the period between 25 June and 27 October 2009 when complete time series from three moored bottom-mounted ADCPs were available. The bottom-mounted ADCPs (1000 kHz Nortek Aquadopp profiler) were deployed at water depths of 23 (A), 10 (B) and 21 m (C), measuring at 4 m depth intervals. This coarse interval was selected to maintain the velocity error < 1 cm s^{-1}, which was used as the observational error in the assimilation system. The original 15-min currents were rotated into model grid components and averaged at 3 h intervals to be consistent with the assimilation steps.

Additionally, three spatial surveys were conducted on 15 July, 27 August and 24 September 2009 with a 1200 kHz RDI Workhorse Sentinel ADCP mounted on an Endeco/YSI 703 V-Fin towed along the stern of a vessel. Currents were recorded along the ADCP transect (Fig. 1) at 1 m depth bin from 4 to 16 m every 1 s and then averaged at 1 min ensembles. These spatial surveys were not assimilated, and they were used to provide independent data set to validate model results. We note that both moored currents and spatial surveys were obtained above the pycnocline located at ~ 25-30 m.

3. Results

Four main model runs were conducted, which included: (1) a simulation without data assimilation and with transports at open boundaries set to zero (CNTRL run), (2) an EAKF simulation with assimilation of moored ADCP time series but without parameter estimation (ASSIM run), (3) an EAKF simulation with assimilation of moored ADCP time series using simultaneous state and parameter estimation (AS+ES run), and (4) a simulation without data assimilation but with estimated transports at open boundaries from the AS+ES run (ESTIM run). In addition, a set of extra model runs were performed to test the sensitivity with respect to: (1) the number of assimilated ADCPS, (2) the assimilation parameters (ensemble size, localization cut-off distance, and inflation factor), (3) the boundary conditions from a regional model (CNTRLnst), (4) the temperature and salinity fields (ESTIMts1 and ESTIMts2 runs), and (5) the initial conditions (AS+ESini). The ensemble mean outputs at 3 h interval from the ASSIM and AS+ES runs were assumed to be the best estimates of the model state and the values at open boundaries (only for AS+ES run). Validation was performed against the current time series from the moored ADCPs and against independent (non-assimilated) spatial surveys of currents from the towed ADCP.

3.1. Comparison of current time series

The time evolution of the low-passed root mean square error (RMSE) in currents over the moored ADCP sites for the four runs is shown in Fig. 3. The ASSIM and AS+ES runs achieved smaller RMSE than the other runs, as they both assimilated the moored ADCPs. The error for the AS+ES run is slightly lower than ASSIM, which is attributed to the parameter estimation (the only difference between these two runs). For the other two runs without data assimilation, ESTIM shows significant improvement over CNTRL, indicating the benefit of using the estimated transports at open boundaries.

Spectral contents were estimated at each moored ADCP site for the observed current time series and the four runs to identify the presence of ITWs in the model simulations. A Hanning window of 160 points (20 days) with half window overlapping was applied for all spectral computations. The spectra are similar for the observed currents and the ASSIM, AS+ES and ESTIM runs (Fig. 4), although ASSIM has less energy at lower frequencies. In contrast, the CNTRL shows no peak at 60 h and a much smaller peak at 24 h. This indcates that the estimated boundary conditions (AS+ES and ESTIM runs) contained information of the large-scale circulation induced by the ITWs.

The time evolution of the estimated low-passed transports at the eastern boundary from the AS+ES run are shown in Fig. 5. The spectral content shows clear peaks at 60 and 24 h, indicative of the presence of ITWs. In addition, the first EOF mode of 3D current perpendicular to the western boundary indicates a first-mode internal Kelvin wave structure, consistent with a first radial ITW mode. According to Jordi et al. (2011), the ITW at 60 h is the first radial and first azimuthal mode, and the ITW at 24 h is the first radial and second azimuthal mode. The estimated transports at the western boundary were similar to the transports at the eastern boundary (the correlation was 0.82). In contrast, the estimated transports were much weaker at the southern (offshore) boundary (not shown). This is consistent with the alongshore propagation of the ITWs.

Given the good agreement between observed currents and the ESTIM run, we analyzed in detail the impact of the estimated boundaries on the circulation and its relation to wind forcing. We computed the canonical correlation analysis (CCA) between winds with low- and daily band-passed currents following the same methodology used by Jordi et al. (2011). We refer the reader to that paper for a detailed description of the

300 method. The CCA finds maximum correlation between two data sets of different
301 variables, in our case winds and currents (Bretherton et al., 1992). Low-passed currents,
302 indicative of the period of 60 h, were computed using a Lanczos filter with a cut-off
303 period of 33 h. Daily band-passed current were also computed using a Lanczos filter
304 between 20 and 28 h.

305 The first CCA mode of low-passed currents represents a uniform circulation parallel to
306 the coast associated with the first radial and first azimuthal ITW mode propagating
307 around Mallorca (Jordi et al., 2011). Model results for the ESTIM run were consistent
308 with observations, for both spatial patterns and temporal amplitude functions (Fig. 6).
309 We note that the CCA results for observed currents were slightly different from those
310 obtained by Jordi et al. (2011) because of a shorter time period (from 25 June to 27
311 October 2009) and longer time step used here to compute the CCA modes. However,
312 the dynamical interpretation of CCA modes remains the same.

313 Significant differences appeared for the second CCA mode of low-passed currents
314 between observed and simulated time series (Fig. 7). Simulated currents were weaker at
315 moorings A and C, and stronger at mooring B. This second CCA mode is also related to
316 the first radial and first azimuthal ITW mode. However, currents entering into the inner
317 bay associated with the ITW are stronger than the first CCA mode and form an
318 anticyclonic gyre over the eastern part of the bay by flow separation (Jordi et al., 2011).
319 This suggests that the AS+ES underestimates the strong inflow at the boundaries.

320 The circulation at the period of 24 h is modulated by remote and local responses to the
321 wind (Jordi et al., 2011). The first CCA mode of daily band-passed currents represents
322 the remotely generated first radial and second azimuthal ITW mode flowing parallel to
323 the coast (Fig. 8). The second CCA mode of daily band-passed represents the local
324 response to the sea breeze with a wind-forced surface transport and a compensating
325 flow below (Fig. 9). Although the agreement between observed and estimated currents
326 was generally good for both CCA modes, there were significant discrepancies at upper
327 levels of moorings A and C. A possible explanation is the lack of realistic heat fluxes in
328 the model simulation, which could generate a more complex vertical structure.

329

330 *3.2. Comparison of spatial surveys*

Moored ADCP data are not independent of ASSIM, AS+ES or ESTIM runs. The ASSIM and AS+ES runs assimilated the moored ADCP data and ESTIM run used the flow at the open boundaries derived from AS+ES. Therefore, we also compared with the spatial surveys of currents from towed ADCP that were not used in any of the model runs. Model outputs from the three runs during the surveys were interpolated into the towed ADCP transect (Fig. 1). Fig. 10 shows the RMSE in currents over the horizontal levels between observed and simulated currents for the three surveys. The RMSE error was similar for ASSIM, AS+ES and ESTIM runs for surveys on 15 July and 24 September 2009, with an overall RMSE of about 45% lower than the CNTRL run. On 27 August 2009, the RMSE was similar for the four runs, although it was slightly lower for the AS+ES run. In all three surveys, the RMSE for ASSIM, AS+ES and ESTIM runs was about 4 cm s^{-1}. This suggests an intrinsic uncertainty of about 4 cm s^{-1} due to missing physics (including surface heat and water fluxes), limited observations, etc...

Figure 10 also includes comparisons of the complex vector correlation coefficients in currents over the horizontal levels between observed and simulated currents for the three surveys. Correlation coefficients for AS+ES run were always > 0.8. Slightly lower values were archived by the ASSIM and ESTIM run. Correlation coefficients for CNTRL run clearly were much worse, with values < 0.5 (except for the deeper level on 24 September 2009). Despite similar RMSE between ASSIM, AS+ES and ESTIM runs, the AS+ES run shows better agreement in spatial pattern.

Detailed comparisons were made between observed and assimilated (ASSIM, AS+ES and ESTIM) currents at 4 m and 16 m depth. Observed currents were interpolated into the model grid using optimal interpolation with a cut-off length scale of 2000 m and model currents were masked out where there were no measurements. For the survey on 15 July 2009, currents delineated a clockwise circulation parallel to the coast (Fig. 11). The flow at 4 and 16 m depth penetrated through the western side of the Bay (around 7-8 km in the *x* direction) and exited at about 3-4 km from the eastern side. All three runs reproduced the inflows near the western side, although currents were underestimated. However, the outflows for ASSIM and ESTIM runs were too strong and much closer to the eastern side, and only AS+ES run resembled the towed ADCP.

On 27 August 2009, observed currents were much weaker (Fig. 12). Small-scale current cells were observed at 4 m depth, whereas the currents at 16 m depth flowed parallel to the coast from east to west. Model runs displayed small-scale currents at 4 m depth, but

364 the agreement with the observation was not very good, especially for ASSIM and
365 ESTIM runs. At 16 m depth, the observed circulation was well reproduced by AS+ES
366 and ESTIM runs, although the outflow currents for ESTIM run were too weak.

367 The circulation on 24 September 2009 at 4 m depth was similar to 15 July 2009 with
368 currents flowing parallel to the coast, although the outflow was located near the eastern
369 side of the Bay (Fig. 13). There was a reasonable agreement for model runs at 4 m depth
370 for this survey. At 16 m depth, observed currents had a clear onshore component.
371 Although ASSIM, AS+ES and ESTIM runs reproduced this onshore flow, currents for
372 ASSIM and ESTIM had currents directed to the east.

373 According to Jordi et al. (2011), currents on 15 July and 24 September 2009 were
374 dominated by the first CCA mode of low-passed currents, while during 27 August 2009
375 ITWs were almost absent. The estimated boundaries account mainly for ITWs; and
376 therefore the good results of AS+ES and ESTIM runs on 15 July and 24 September
377 2009 are not surprising. The best agreement is for AS+ES, which combines assimilation
378 and estimation of boundary conditions. On the other hand, on 27 August 2009 the
379 small-scale currents dominated especially at upper levels. These small-scale currents are
380 likely responsible for the inherent uncertainty, suggesting that the observational network
381 (3 moored ADCPs) is not sufficient to resolve small-scale patterns through data
382 assimilation.

383

384 *3.3. Estimation of boundary condition with different number of ADCPs*

385 The estimation of boundary conditions using three moored bottom-mounted ADCPs
386 significantly improves the model results, although there is an intrinsic uncertainty. To
387 find out whether this uncertainty is caused by the observational network design, we
388 repeated the AS+ES run assimilating a different number of ADCPs. The estimated
389 boundary conditions then were used in separated simulations to force the ESTIM run,
390 similar to the case described earlier.

391 Table 1 shows the RMSE averaged over the three moored ADCP current time series and
392 for the first two CCA modes of low- and daily band-passed currents between observed
393 and simulated (ESTIM) currents using different number of assimilated ADCPs. In
394 general, the model error was reduced as more ADCPs were used to estimate the
395 boundary conditions. In addition, when the same number of ADCPs were assimilated

396 results were better in the cases where ADCP B was not used. We note that ADCPs A
397 and C were closer to the open boundaries and had more vertical levels. Consequently,
398 ADCP A or C had more impact especially on the open boundaries. The exception was
399 the second CCA mode for the low-passed currents, where results using the ADCP B
400 were sometimes better than using the other ADCPs. This second CCA mode for the
401 low-passed currents is related to an anticyclonic gyre in the eastern part of the bay;
402 therefore ADCP B can provide more information about this gyre than ADCP A. This
403 indicates that the observational network design is important to correctly estimate the
404 boundary conditions.

405 Table 2 shows the RMSE for spatial surveys. The impact of the number of ADCPs used
406 to estimate boundary conditions was significant on 15 July and 24 September 2009 for
407 both AS+ES and ESTIM runs. The error levels however did not depend significantly on
408 the number of ADCPs on 27 August 2009. This confirms that a background uncertainty
409 of about 4 cm s^{-1} exists. When the ITWs did not dominate and circulation was weak (on
410 27 August 2009), model error remained in the order of the uncertainty. However, the
411 benefit of estimated boundaries was significant when circulation was controlled by the
412 ITWs.

413

414 *3.4. Sensitivity runs*

415 Several sensitivity experiments were conducted concerning the setup of the EAKF. In
416 ensemble based data assimilation methods, the ensemble size is an important parameter.
417 When ensemble size is too small, errors are introduced in the covariance estimates,
418 which lead to erroneous corrections of the model state. We run several simulations
419 varying the ensemble size, from 4 to 64 members. Results of the AS+ES run did not
420 vary significantly for ensemble sizes larger than 20 members; although an ensemble size
421 of 32 members was selected in this study.

422 Another issue related to smaller ensemble size is the covariance estimates having too
423 large amplitudes at long distances. To avoid this issue, we localized the impact of the
424 observations by multiplying the Kalman gain with a covariance cut-off distance of 2
425 km. However, results were similar for cut-off distances ranging from 2 to 25 km (the
426 length of the model domain). For larger model domains, results might be more sensitive
427 to the localization length scale.

The variances of boundary values after each assimilation step were multiplied by an inflation factor so that posterior and prior variances of boundary values were equal. Inflation values lower (posterior variance lower than prior variance) or greater (posterior greater than prior) than the selected value had negative impact on model results. In our model runs the ensemble variance depends exclusively on the variance of boundary values, so that a progressive decrease in the posterior variance leads to a null ensemble variance with time (filter divergence). On the other hand, the increment of posterior variance at each assimilation step increases progressively the variances of boundary values, so that transports at the boundaries become unrealistic large and the model blows up.

In the CNTRL run, transports at open boundaries were set to zero because there is no real information about the transports in this area. However, Jordi et al. (2011) simulated the circulation in the Palma Bay for the same period with a regional model that included the entire Balearic Islands. We therefore run a new simulation one-way nested to this regional model and without data assimilation (CNTRLnst run) to include the large-scale forcing. Current spectra for this run showed a peak at 60 h (not shown), indicating the presence of ITWs. However, as shown in Fig. 14a, while CNTRLnst run was slightly better than CNTRL, ESTIM was still much better. This highlights the challenge in model nesting when the large scale model might not produce the correct open boundary conditions for the coastal model.

The circulation in the Palma Bay was mainly driven by the ITWs, and the temperature and salinity were mostly uniform above the thermocline during the study period (Jordi et al., 2011). We have focused our analysis on currents and not on temperature and salinity fields, and in all previous runs the initial fields of temperature and salinity were horizontally uniform based on summer climatology (Fig. 2). To analyze the impact of temperature and salinity, we performed 2 new simulations similar to the AS+ES run: (1) with temperature and salinity fields held fixed during the simulation (equal to the initial condition, AS+ESts1) and (2) including the estimation of transports, temperature and salinity at the open boundaries (AS+ESts2). The estimated boundaries from these 2 runs were used to force new ESTIM runs (ESTIMts1 and ESTIMts2, respectively). The RMSE for these 2 runs was quite similar to ESTIM (Fig. 14b). Nevertheless, the error was slightly better when estimated temperature and salinity at the open boundaries were

460 used (ESTIMts2 run). This confirms that temperature and salinity had a slight
461 contribution to the circulation of the Palma Bay, at least during the study period.

462 In the previous simulations, velocities were initialized from rest. We performed an
463 EAKF simulation where 32 initial current fields were created by sampling the AS+ES
464 run at random times (AS+ESini run). This initialization ensures that initial ensembles
465 are representative of the full ocean phase space. Differences between AS+ESini and
466 AS+ES appeared during the first days of simulation due to initial conditions (Fig. 15).
467 After ~2 to 3 days, differences were almost negligible, indicating that the flow is driven
468 by boundary conditions (ITWs) and wind forcing.

469 Fig. 15 also shows the impact of each assimilation step on the model results. The RMSE
470 of the analysis (posterior) estimate is always lower than the corresponding forecast
471 (prior) estimate, indicating good performance of the assimilation system. The
472 differences in RMSE between forecast and analysis estimates though are small. This is
473 due to the frequency of assimilation (3 h) much shorter compared to the time scales of
474 the dominant motions (24 and 60 h). With longer time between assimilation steps, the
475 RMSE of forecast will be larger and the correction caused by the assimilation more
476 pronounced.

477

478 **4. Discussion and Conclusions**

479 The EAKF was used to estimate the volume transports at the open boundaries in a
480 coastal ocean model of the Palma Bay through simultaneous state and parameter
481 estimation. The AS+ES assimilated velocity time series from three moored ADCPs in
482 the inner part of the Bay to correct the model state and estimate the transport at the open
483 boundaries every three hours in a three-month period from 25 June to 27 October 2009.
484 To evaluate model results, additional model simulations were performed without
485 parameter estimation (ASSIM) and without data assimilation but with the open
486 boundary values updated from the AS+ES (ESTIM). These simulations produced
487 significant improvement with respect to simulation using prescribed open boundary
488 values (CNTRL) when validated with the velocity time series and spatial velocity fields.

489 Despite the improvement, some errors remained as an inherent uncertainty. For
490 example, model errors for the four runs were similar on 27 August where currents were
491 not influenced by the boundary conditions, although the spatial patterns were improved

492 in the assimilated runs. The comparison of model simulations with boundary conditions
493 estimated from the assimilation of one, two or three ADCPs reveals that the number and
494 location of the assimilated ADCPs is important to capture some small-scale patterns
495 such as the eddy generated in the eastern part of the Bay (second CCA mode of low-
496 passed currents). This suggests that more ADCPs are required to reproduce the small-
497 scale patterns. In addition, other physical processes such as coastal fronts and freshwater
498 discharges have a small contribution to the coastal currents (Jordi et al., 2011).
499 Inclusion of temperature/salinity data, surface heat fluxes and freshwater discharges
500 should also improve the model results.

501 Transports at the open boundaries were determined through simultaneous state and
502 parameter estimation. The model state vector was augmented with the boundary
503 condition values. The EAKF updated the boundary conditions by relating linearly the
504 regular state vector to the flow at the boundaries through the covariance matrix. No
505 other constraint was imposed to the boundary condition. This could cause dynamical
506 inconsistencies as the inflow/outflow is not conserved at each assimilation step.
507 However, this is not a problem as long as the covariance structure has a sufficiently
508 strong dependence between the regular state variables and the estimated parameters
509 (boundaries), as it is in our study. This avoids unrealistic values for the estimated
510 parameters.

511 Several previous model studies addressed the estimation of boundary conditions using
512 variational techniques (Edwards et al., 2004; Hoteit et al., 2009; Taillandier et al.,
513 2004). These techniques are based on minimization of a cost function, which could
514 suffer from the problems of converging to local minima. In contrast, the EAKF is a
515 statistical minimization based on the covariance between observed variables, model
516 state and estimated parameters in the ensemble. On the other hand, the convergence of
517 the ensemble members as a consequence of the assimilation may result in a small
518 variance that the observations are basically ignored and estimated parameters tend to a
519 constant value. The inflation of parameters after each assimilation step is thus required
520 to avoid filter divergence. We note that this inflation technique increases only the
521 variance of parameters and does not modify the mean value, which is considered as the
522 best estimate.

523 Simultaneous state and parameter estimation with ensemble data assimilation also had
524 been used to estimate parameters in regional or coastal domains, including boundary

conditions either as augmented state variables (Cossarini et al., 2009; Lermusiaux, 1999) or their actual mathematical formulation (Lermusiaux, 2007). These studies were based on the error subspace statistical estimation (ESSE), which uses the dominant eigen-decompositions of error covariance matrices to reduce the error statistics given by the ensembles. Our study focused on the open boundary conditions as the unique source of model error motivated by the observational studies. We specifically evaluated the capability of the system to estimate the boundary conditions: the results using the open boundary values updated from the EAKF without data assimilation (ESTIM run) significantly improved the results using prescribed open boundary values (CNTRL run). Also, validation with independent spatial velocity survey data perhaps is unique among all previous model studies with estimation of open boundary conditions.

Finally, this study was limited in scope to the estimation of flow at open boundaries because circulation in the Palma Bay depends mainly on ITW induced currents. We nevertheless believe that our EAKF system will be well suited for estimation of the whole boundary values. In fact, the sensitivity AS+ESts2 run includes the estimation of transports, temperature and salinity at the open boundaries. Furthermore, the results obtained suggests promising possibility for more generalized estimation problems, such as values to obtain better-performing small-scale atmospheric forcing, freshwater discharges, or other physics parameterizations (bottom friction, turbulent parameters, etc.).

Acknowledgments

This research utilized resources at the New York Center for Computational Sciences at Stony Brook University/Brookhaven National Laboratory which was supported by the U.S. Department of Energy under Contract No. DE-AC02-98CH10886 and by the State of New York. This work was partly supported by EDASE (CGL2008-00047/BTE), EHRE (CTM2009-08270) and Platja de Palma projects. A. Jordi's work was supported by a Ramón y Cajal grant from the Spanish Ministry of Economy and Competitiveness. We are grateful to AEMET for providing meteorological data.

References

Aksoy, A., Zhang, F.Q., Nielsen-Gammon, J.W., 2006. Ensemble-based simultaneous state and parameter estimation with MM5. Geophys Res Lett 33.

Anderson, J.L., 2001. An ensemble adjustment Kalman filter for data assimilation. Mon Weather Rev 129, 2884-2903.

Anderson, J.L., 2003. A local least squares framework for ensemble filtering. Mon Weather Rev 131, 634-642.

Anderson, J.L., Anderson, S.L., 1999. A Monte Carlo implementation of the nonlinear filtering problem to produce ensemble assimilations and forecasts. Mon Weather Rev 127, 2741-2758.

Anderson, J.L., Collins, N., 2007. Scalable implementations of ensemble filter algorithms for data assimilation. J Atmos Ocean Tech 24, 1452-1463.

Auclair, F., Marsaleix, P., De Mey, P., 2003. Space-time structure and dynamics of the forecast error in a coastal circulation model of the Gulf of Lions. Dynam Atmos Oceans 36, 309-346.

Barth, A., Alvera-Azcarate, A., Beckers, J.M., Rixen, M., Vandenbulcke, L., 2007. Multigrid state vector for data assimilation in a two-way nested model of the Ligurian Sea. J Marine Syst 65, 41-59.

Barth, A., Alvera-Azcarate, A., Rixen, M., Beckers, J.M., 2005. Two-way nested model of mesoscale circulation features in the Ligurian Sea. Prog Oceanogr 66, 171-189.

Bretherton, C.S., Smith, C., Wallace, J.M., 1992. An Intercomparison of Methods for Finding Coupled Patterns in Climate Data. J Climate 5, 541-560.

Brink, K.H., 1999. Island-trapped waves, with application to observations off Bermuda. Dynam Atmos Oceans 29, 93-118.

Cailleau, S., Fedorenko, V., Barnier, B., Blayo, E., Debreu, L., 2008. Comparison of different numerical methods used to handle the open boundary of a regional ocean circulation model of the Bay of Biscay. Ocean Model 25, 1-16.

Cossarini, G., Lermusiaux, P.F.J., Solidoro, C., 2009. Lagoon of Venice ecosystem: Seasonal dynamics and environmental guidance with uncertainty analyses and error subspace data assimilation. J Geophys Res-Oceans 114.

587 Chapman, D.C., 1985. Numerical treatment of cross-shelf open boundaries in a
588 barotropic coastal ocean model. J Phys Oceanogr 15, 1060-1075.

589 Chu, P.C., Fan, C.W., Ehret, L.L., 1997. Determination of open boundary conditions
590 with an optimization method. J Atmos Ocean Tech 14, 723-734.

591 Debreu, L., Blayo, E., 2008. Two-way embedding algorithms: a review. Ocean
592 Dynamics 58, 415-428.

593 Edwards, C.A., Fake, T.A., Codiga, D.L., Bogden, P.S., 2004. Spring-summer
594 frontogenesis at the mouth of Block Island Sound: 2. Combining acoustic Doppler
595 current profiler records with a general circulation model to investigate the impact of
596 subtidal forcing. J Geophys Res-Oceans 109.

597 Evensen, G., 1994. Sequential data assimilation with a nonlinear quasi-geostrophic
598 model using Monte-Carlo methods to forecast error statistics. J Geophys Res-Oceans
599 99, 10143-10162.

600 Evensen, G., 2009. The Ensemble Kalman Filter for Combined State and Parameter
601 Estimation: Monte Carlo Techniques for Data Assimilation in Large Systems. Ieee
602 Control Systems Magazine 29, 83-104.

603 Gaspari, G., Cohn, S.E., 1999. Construction of correlation functions in two and three
604 dimensions. Q J Roy Meteor Soc 125, 723-757.

605 Greatbatch, R.J., Otterson, T., 1991. On the formulation of open boundary conditions at
606 the mouth of a bay. J Geophys Res-Oceans 96, 18431-18445.

607 Haley, P.J., Jr., Lermusiaux, P.F.J., 2010. Multiscale two-way embedding schemes for
608 free-surface primitive equations in the "Multidisciplinary Simulation, Estimation and
609 Assimilation System". Ocean Dynamics 60, 1497-1537.

610 Haley, P.J., Jr., Lermusiaux, P.F.J., Robinson, A.R., Leslie, W.G., Logoutov, O.,
611 Cossarini, G., Liang, X.S., Moreno, P., Ramp, S.R., Doyle, J.D., Bellingham, J.,
612 Chavez, F., Johnston, S., 2009. Forecasting and reanalysis in the Monterey
613 Bay/California Current region for the Autonomous Ocean Sampling Network-II
614 experiment. Deep-Sea Res Pt Ii 56, 127-148.

615 Hoteit, I., Cornuelle, B., Kim, S.Y., Forget, G., Koehl, A., Terrill, E., 2009. Assessing
616 4D-VAR for dynamical mapping of coastal high-frequency radar in San Diego. Dynam
617 Atmos Oceans 48, 175-197.

618 Ide, K., Courtier, P., Ghil, M., Lorenc, A.C., 1997. Unified notation for data
619 assimilation: Operational, sequential and variational. Journal of the Meteorological
620 Society of Japan 75, 181-189.

621 Jan, S., Wang, Y.H., Wang, D.P., Chao, S.Y., 2004. Incremental inference of boundary
622 forcing for a three-dimensional tidal model: tides in the Taiwan Strait. Cont Shelf Res
623 24, 337-351.

624 Jazwinski, A.H., 1970. Stochastic Processes and Filtering Theory, New York.

625 Jones, J.E., Davies, A.M., 2003. On combining current observations and models to
626 investigate the wind induced circulation of the eastern Irish Sea. Cont Shelf Res 23,
627 415-434.

628 Jordi, A., Basterretxea, G., Anglès, S., 2009a. Influence of ocean circulation on
629 phytoplankton biomass distribution in the Balearic Sea: Study based on Sea-viewing
630 Wide Field-of-view Sensor and altimetry satellite data. J Geophys Res-Oceans 114,
631 doi:10.1029/2009JC005301.

632 Jordi, A., Basterretxea, G., Wang, D.P., 2009b. Evidence of sediment resuspension by
633 island trapped waves. Geophys Res Lett 36, doi:10.1029/2009GL040055.

634 Jordi, A., Basterretxea, G., Wang, D.P., 2011. Local versus remote wind effects on the
635 coastal circulation of a microtidal bay in the Mediterranean Sea. J Marine Syst 88, 312-
636 322.

637 Jordi, A., Wang, D.-P., 2012. sbPOM: A parallel implementation of Princenton Ocean
638 Model. Environmental Modelling & Software 38, 59-61.

639 Korres, G., Hoteit, I., Triantafyllou, G., 2007. Data assimilation into a Princeton Ocean
640 Model of the Mediterranean Sea using advanced Kalman filters. J Marine Syst 65, 84-
641 104.

642 Korres, G., Nittis, K., Hoteit, I., Triantafyllou, G., 2009. A high resolution data
643 assimilation system for the Aegean Sea hydrodynamics. J Marine Syst 77, 325-340.

644 Lermusiaux, P.F.J., 1999. Estimation and study of mesoscale variability in the Strait of
645 Sicily. Dynam Atmos Oceans 29, 255-303.

646 Lermusiaux, P.F.J., 2007. Adaptive modeling, adaptive data assimilation and adaptive
647 sampling. Physica D 230, 172-196.

Lermusiaux, P.F.J., Chiu, C.-S., Gawarkiewicz, G.G., Abbot, P., Robinson, A.R., Miller, R.N., Haley, P.J., Leslie, W.G., Majumdar, S.J., Pang, A., Lekien, F., 2006. Quantifying Uncertainties in Ocean Predictions. Oceanography 19, 92-105.

Lermusiaux, P.F.J., Robinson, A.R., 1999. Data assimilation via error subspace statistical estimation. Part I: Theory and schemes. Mon Weather Rev 127, 1385-1407.

Marchesiello, P., McWilliams, J.C., Shchepetkin, A., 2001. Open boundary conditions for long-term integration of regional oceanic models. Ocean Model 3, 1-20.

Marsaleix, P., Auclair, F., Estournel, C., 2006. Considerations on open boundary conditions for regional and coastal ocean models. J Atmos Ocean Tech 23, 1604-1613.

Mellor, G., 1993. Users Guide for a Three-Dimensional, Primitive Equation, Numerical Ocean Model.

Oddo, P., Pinardi, N., 2008. Lateral open boundary conditions for nested limited area models: A scale selective approach. Ocean Model 20, 134-156.

Palma, E.D., Matano, R.P., 1998. On the implementation of passive open boundary conditions for a general circulation model: The barotropic mode. J Geophys Res-Oceans 103, 1319-1341.

Palma, E.D., Matano, R.P., 2000. On the implementation of open boundary conditions for a general circulation model: The three-dimensional case. J Geophys Res-Oceans 105, 8605-8627.

Rixen, M., Book, J.W., Carta, A., Grandi, V., Gualdesi, L., Stoner, R., Ranelli, P., Cavanna, A., Zanasca, P., Baldasserini, G., Trangeled, A., Lewis, C., Trees, C., Grasso, R., Giannechini, S., Fabiani, A., Merani, D., Berni, A., Leonard, M., Martin, P., Rowley, C., Hulbert, M., Quaid, A., Goode, W., Preller, R., Pinardi, N., Oddo, P., Guarnieri, A., Chiggiato, J., Carniel, S., Russo, A., Tudor, M., Lenartz, F., Vandenbulcke, L., 2009. Improved ocean prediction skill and reduced uncertainty in the coastal region from multi-model super-ensembles. J Marine Syst 78, S282-S289.

Shulman, I., Lewis, J.K., Mayer, J.G., 1999. Local data assimilation in the estimation of barotropic and baroclinic open boundary conditions. J Geophys Res-Oceans 104, 13667-13680.

677 Taillandier, V., Echevin, V., Mortier, L., Devenon, J.L., 2004. Controlling boundary
678 conditions with a four-dimensional variational data-assimilation method in a non-
679 stratified open coastal model. Ocean Dynamics 54, 284-298.

680

681

682

683 **Figure captions**

684 Figure 1. (a) Bathymetry (m, gray lines) around the Balearic Islands (western
685 Mediterranean Sea) showing the model domain at the Palma Bay (thick black line). (b)
686 Bathymetry (m, gray lines) in the Palma Bay showing the position of bottom-mounted
687 ADCPs (solid squares) and the track during the towed ADCP surveys (black line).

688 Figure 2. Initial profiles of salinity (PSU, black line) and temperature (ºC, gray line).

689 Figure 3. Low-passed mean RMSE of currents (cm s^{-1}) over the moored ADCP sites for
690 the CNTRL run (red line), the ASSIM run (green line), the AS+ES run (blue line), and
691 the ESTIM run (black line).

692 Figure 4. Current spectra (m^2 s^{-1}) for the alongshore current components over the
693 moored ADCP sites for the CNTRL run (red line), the ASSIM run (green line), the
694 AS+ES run (blue line), the ESTIM run (black line), and the observed current time series
695 (magenta line). Vertical gray lines represent periods of 60 and 24 h.

696 Figure 5. Estimated normal flow from AS+ES run at the eastern open boundary: (a)
697 time evolution of low-passed depth-averaged currents (cm s^{-1}), (b) spectra (m^2 s^{-1}) of
698 depth-averaged currents, and (c) first EOF mode of currents.

699 Figure 6. First CCA mode of low-passed currents: (a) spatial pattern for observed
700 current time series, (b) spatial mode for ESTIM run at moored ADCP sites, and (c)
701 temporal amplitude functions for observed current time series (red line) and ESTIM run
702 at moored ADCP sites (black line). Depths of each current vector are marked (in m).

703 Figure 7. Second CCA mode of low-passed currents: (a) spatial pattern for observed
704 current time series, (b) spatial mode for ESTIM run at moored ADCP sites, and (c)
705 temporal amplitude functions for observed current time series (red line) and ESTIM run
706 at moored ADCP sites (black line). Depths of each current vector are marked (in m).

707 Figure 8. First CCA mode of band-passed currents: (a) spatial pattern for observed
708 current time series, (b) spatial mode for ESTIM run at moored ADCP sites, and (c)
709 temporal amplitude functions for observed current time series (red line) and ESTIM run
710 at moored ADCP sites (black line). Depths of each current vector are marked (in m).

711 Figure 9. Second CCA mode of band-passed currents: (a) spatial pattern for observed
712 current time series, (b) spatial mode for ESTIM run at moored ADCP sites, and (c)

713 temporal amplitude functions for observed current time series (red line) and ESTIM run
714 at moored ADCP sites (black line). Depths of each current vector are marked (in m).

715 Figure 10. Mean RMSE of currents (cm s^{-1}, upper panels) and correlation coefficient
716 (lower panels) over the horizontal levels between the observed currents from the towed
717 ADCP on 15 July (left), 27 August (middle), and 24 September 2009 (right) and the
718 CNTRL run (red line), the ASSIM run (green line), the AS+ES run (blue line), and the
719 ESTIM run (black line).

720 Figure 11. Currents at depths of 4 m (black vectors) and 16 m (red vectors) on 15 July
721 2009 from (a) towed ADCP, (b) ASSIM run, (c) AS+ES run, and (d) ESTIM run.
722 Current vectors are plotted at every third grid point.

723 Figure 12. Currents at depths of 4 m (black vectors) and 16 m (red vectors) on 27
724 August 2009 from (a) towed ADCP, (b) ASSIM run, (c) AS+ES run, and (d) ESTIM
725 run. Current vectors are plotted at every third grid point.

726 Figure 13. Currents at depths of 4 m (black vectors) and 16 m (red vectors) on 24
727 September 2009 from (a) towed ADCP, (b) ASSIM run, (c) AS+ES run, and (d)
728 ESTIM run. Current vectors are plotted at every third grid point.

729 Figure 14. Low-passed mean RMSE of currents (cm s^{-1}) over the moored ADCP sites
730 for (a) the CNTRL run (red line), CNTRLnst run (blue line), and the ESTIM run (black
731 line), and (b) the ESTIM run (black line), the ESTIMts1 run (red line), and the
732 ESTIMts2 run (red line).

733 Figure 15. (a) Mean RMSE of currents (cm s^{-1}) over the moored ADCP sites during the
734 first 4 days for (a) the AS+ES run (black line) and the AS+ESini run (red line), and (b)
735 mean RMSE difference between forecast and analysis for both runs.

736

737

738 **Tables**

739 Table 1. Root mean square errors (RMSE, cm s^{-1}) averaged for the current time series
740 from the three moored ADCPs and for the first two CCA modes of low- and daily band-
741 passed currents between observed and simulated currents using different number of
742 assimilated ADCPs.

Run	Assimilated ADCPs	Average	Low-passed currents		Daily band-passed currents	
			CCA 1	CCA 2	CCA 1	CCA 2
CNTRL	-	6.90	7.38	4.76	3.43	2.28
ESTIM	A	5.68	5.77	5.08	2.48	1.97
ESTIM	B	6.30	6.96	4.28	3.19	2.11
ESTIM	C	5.61	6.73	3.91	2.50	1.87
ESTIM	AB	5.77	5.83	4.14	2.44	1.72
ESTIM	AC	4.98	4.99	4.12	2.38	1.67
ESTIM	BC	5.24	5.94	2.63	2.42	1.71
ESTIM	ABC	4.64	4.80	2.17	2.08	1.27

743

744 Table 2. Root mean square errors (RMSE, cm s^{-1}) for the three spatial surveys between
745 observed and simulated currents using different number of assimilated ADCPs.

Run	Assimilated ADCPs	Jul 15	Aug 27	Sep 24
CNTRL	-	8.68	4.44	7.05
AS+ES	A	4.91	4.90	4.99
AS+ES	B	6.60	3.93	5.46
AS+ES	C	5.18	4.32	5.05
AS+ES	AB	5.37	4.16	4.38
AS+ES	AC	4.68	4.17	3.87
AS+ES	BC	5.32	4.09	4.14
AS+ES	ABC	4.53	3.76	3.86
ESTIM	A	5.81	4.96	5.12
ESTIM	B	6.38	4.39	6.56
ESTIM	C	6.03	4.82	5.29
ESTIM	AB	6.09	4.82	4.63
ESTIM	AC	5.42	4.63	4.33
ESTIM	BC	5.43	4.36	5.27

	ESTIM	ABC	4.93	4.43	3.91

746

747

Figure 1
Click here to download Figure: fig01.eps

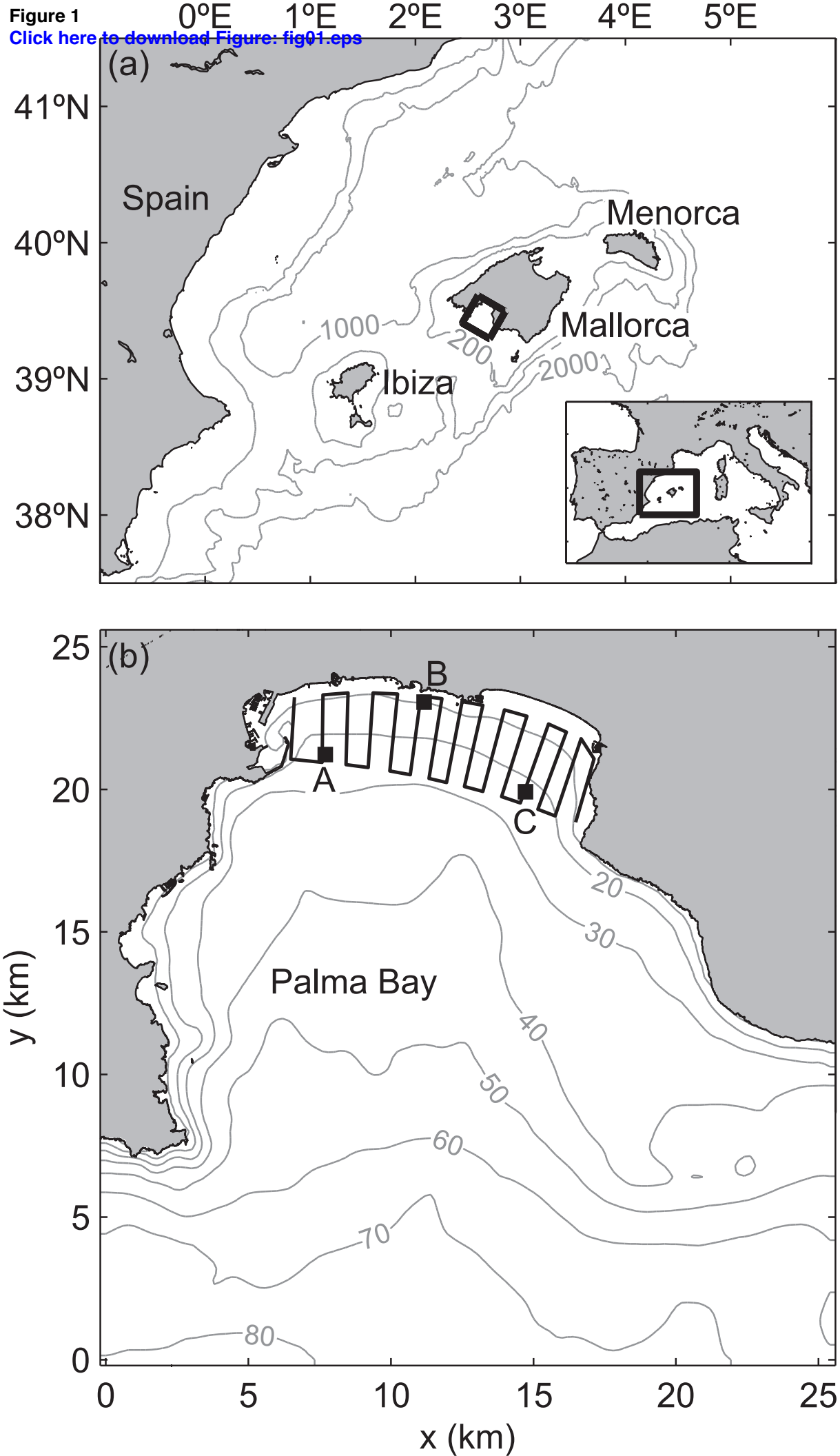

Figure 2
Click here to download Figure: fig02.eps

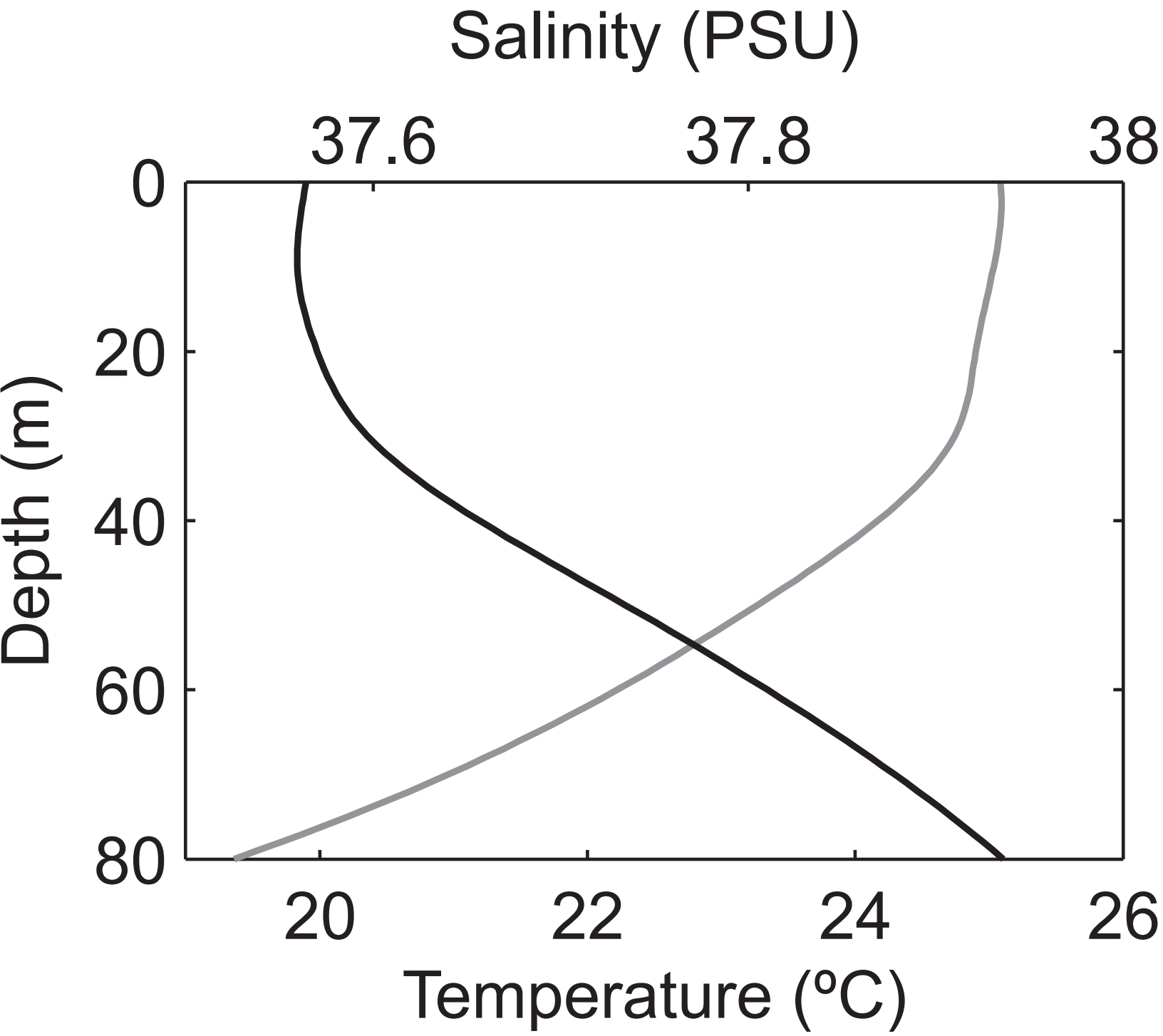

Figure 3
Click here to download Figure: fig03.eps

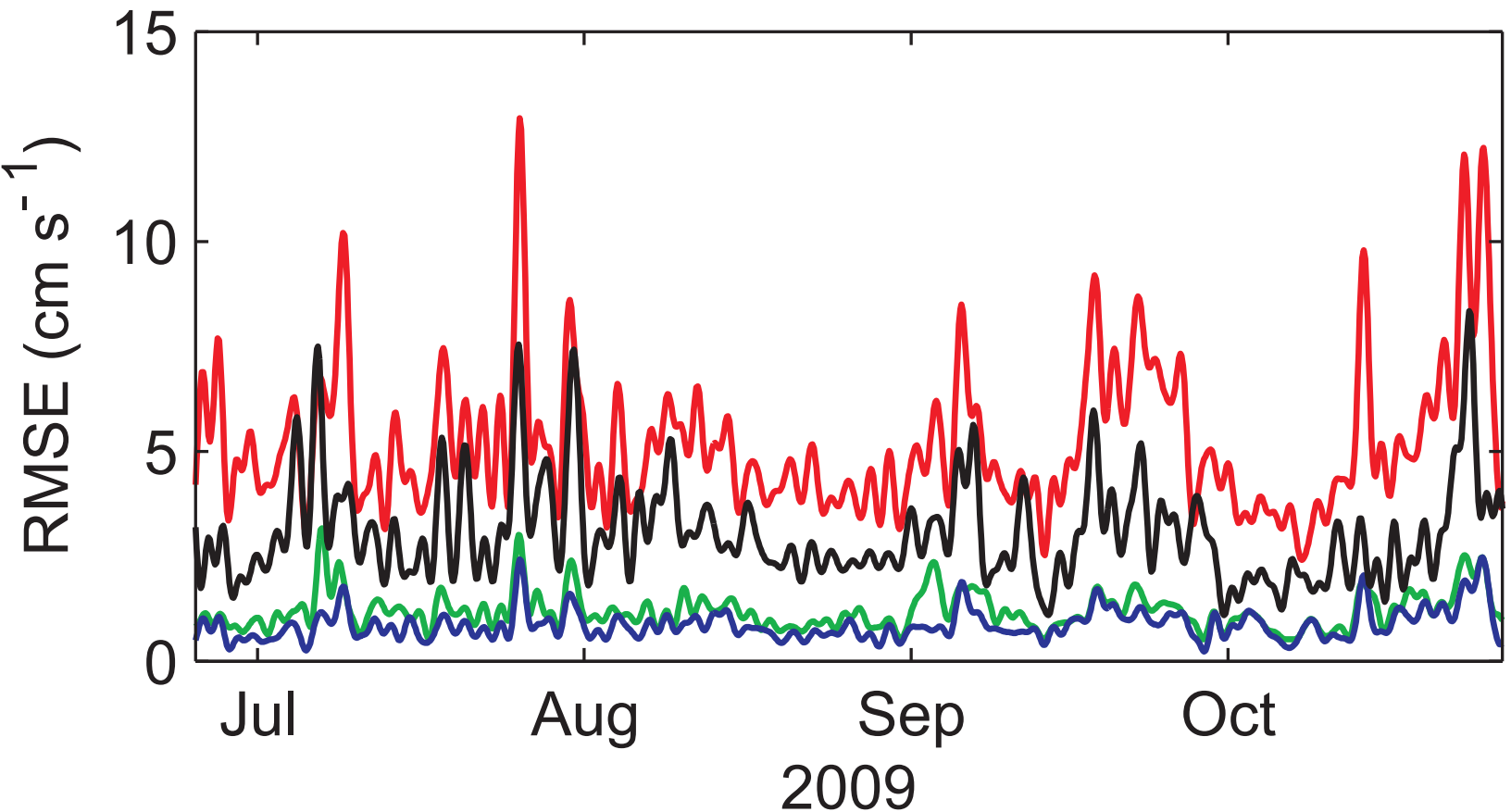

Figure 4
Click here to download Figure: fig04.eps

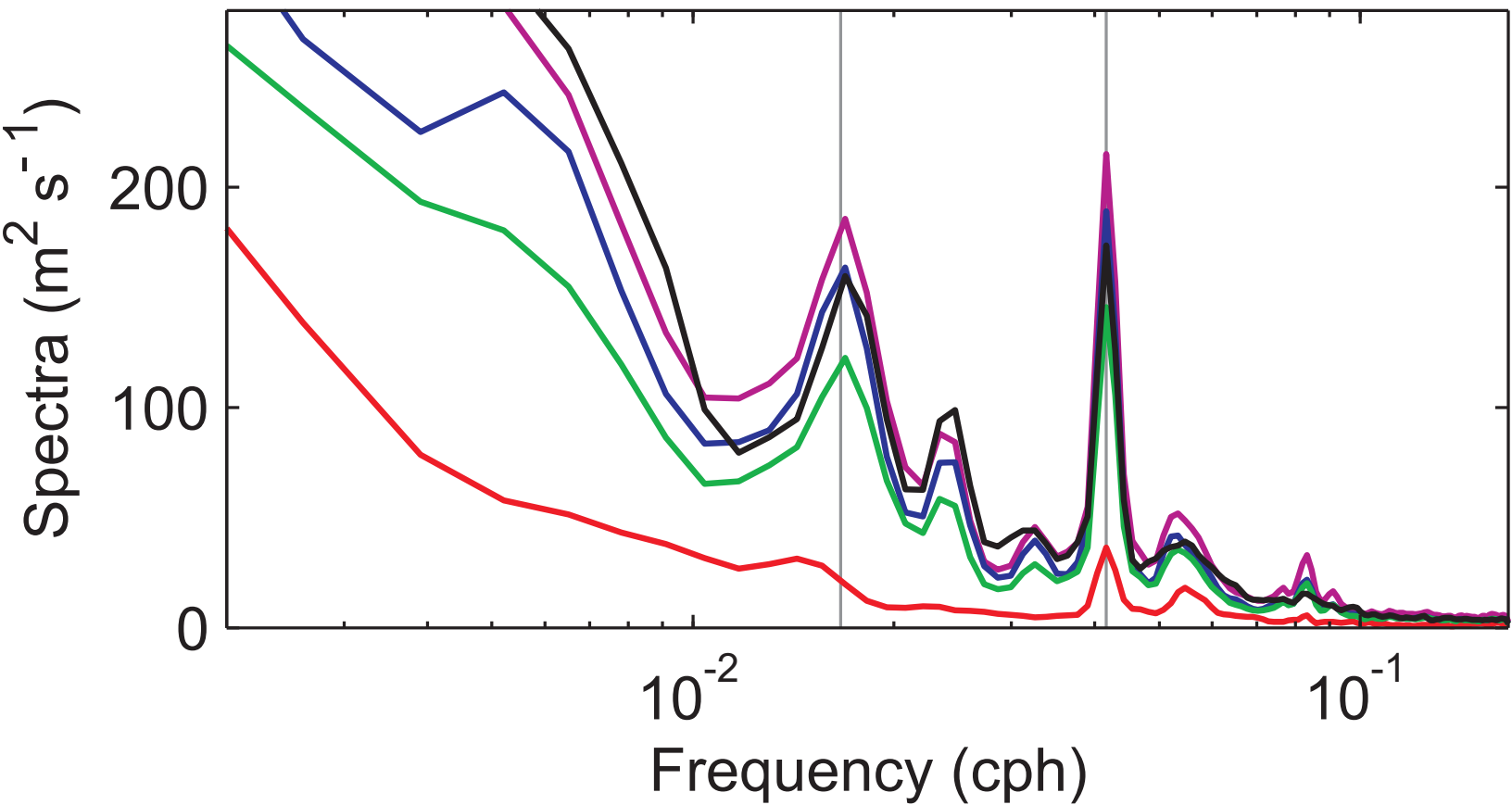

Figure 5
Click here to download Figure: fig05.eps

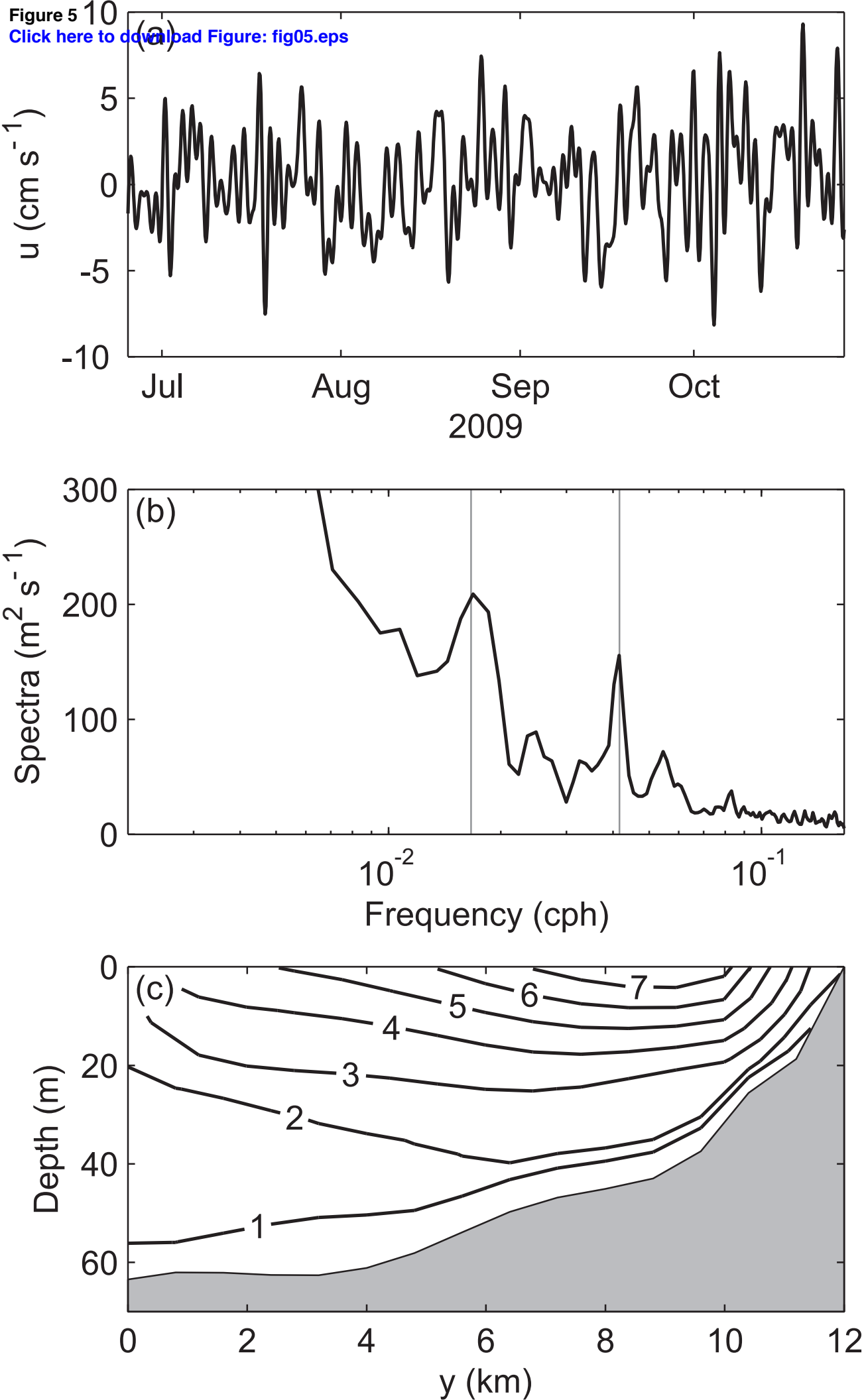

Figure 6
Click here to download Figure: fig06.eps

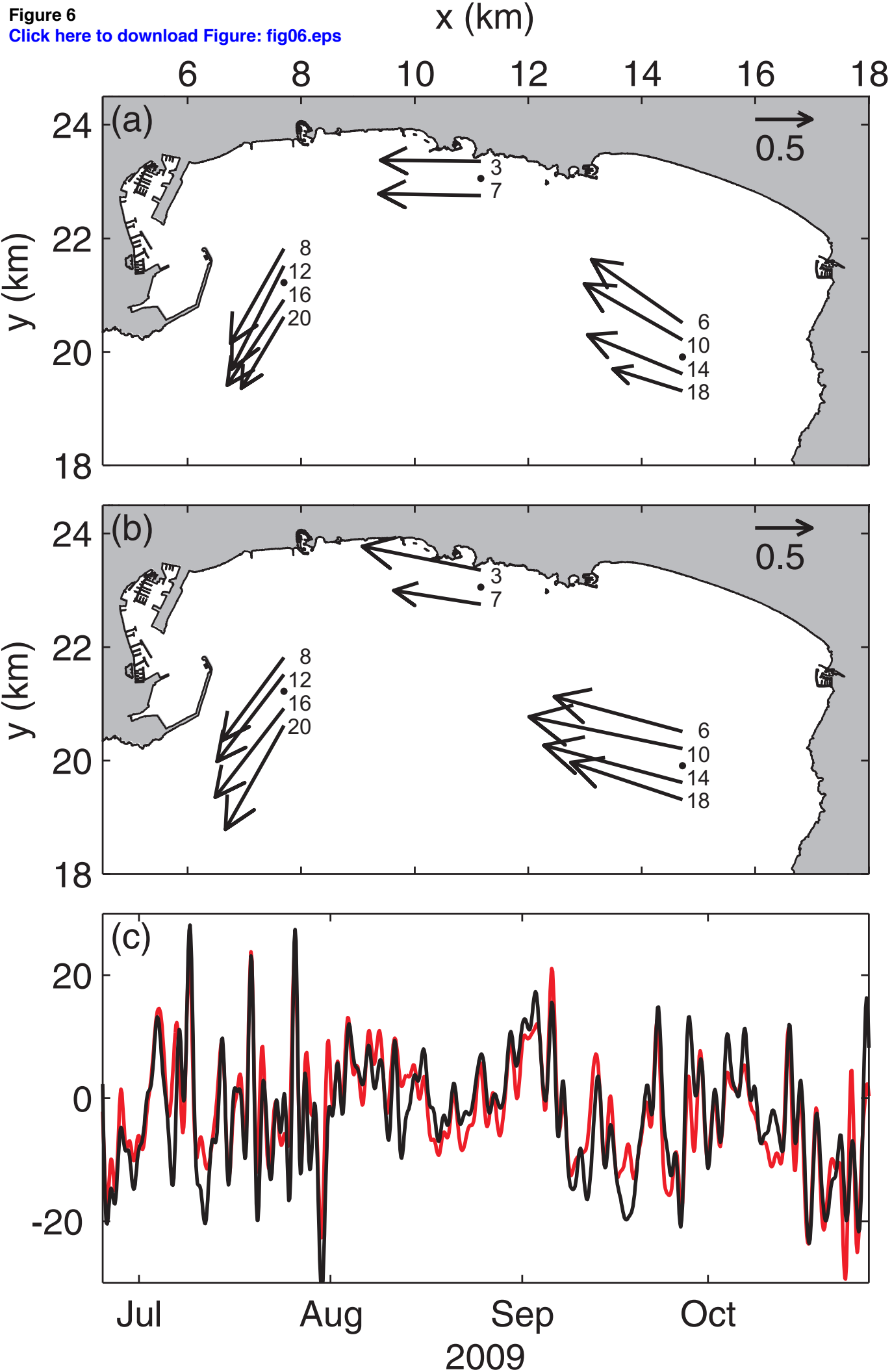

Figure 7
Click here to download Figure: fig07.eps

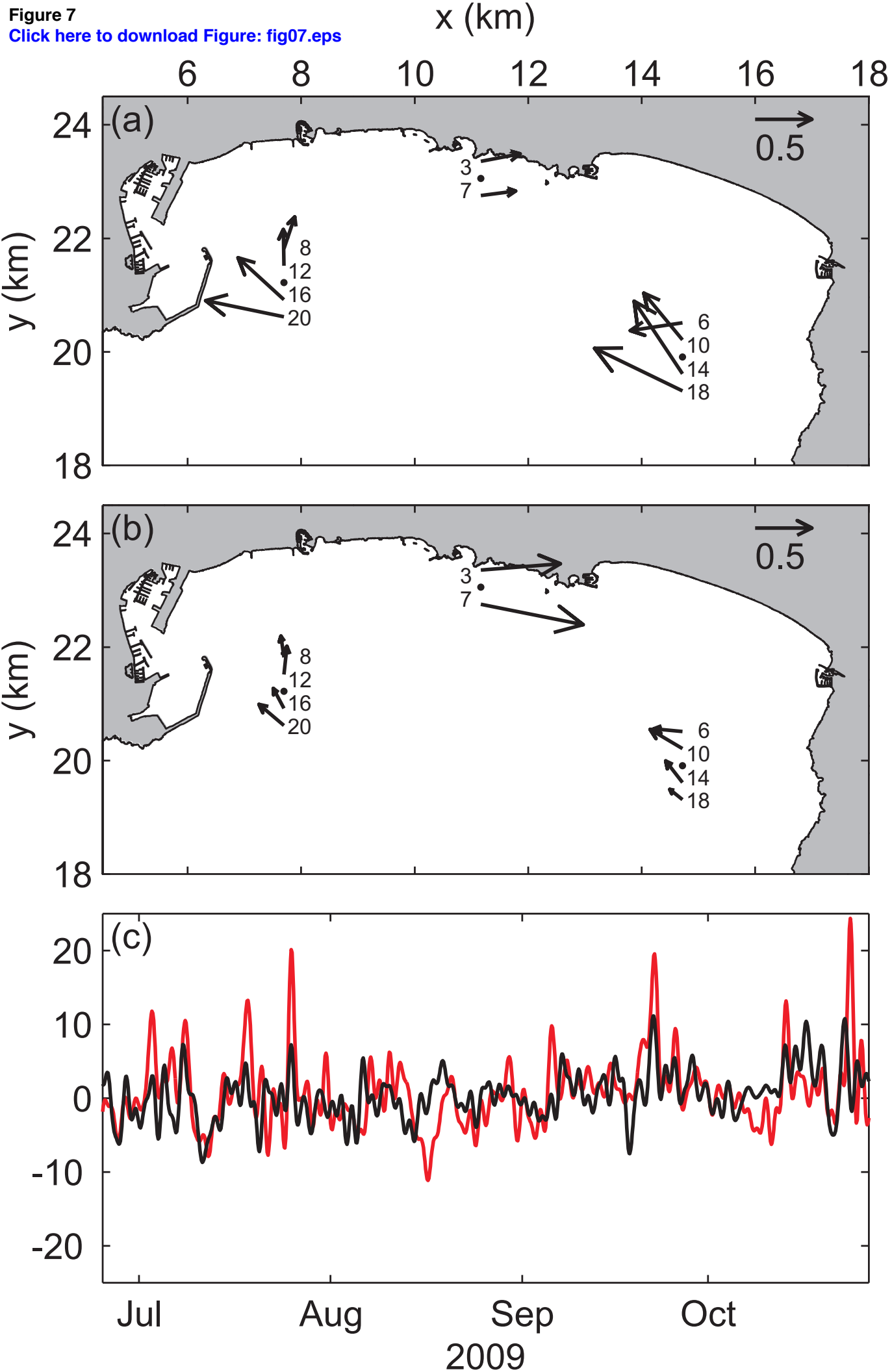

Figure 8
Click here to download Figure: fig08.eps

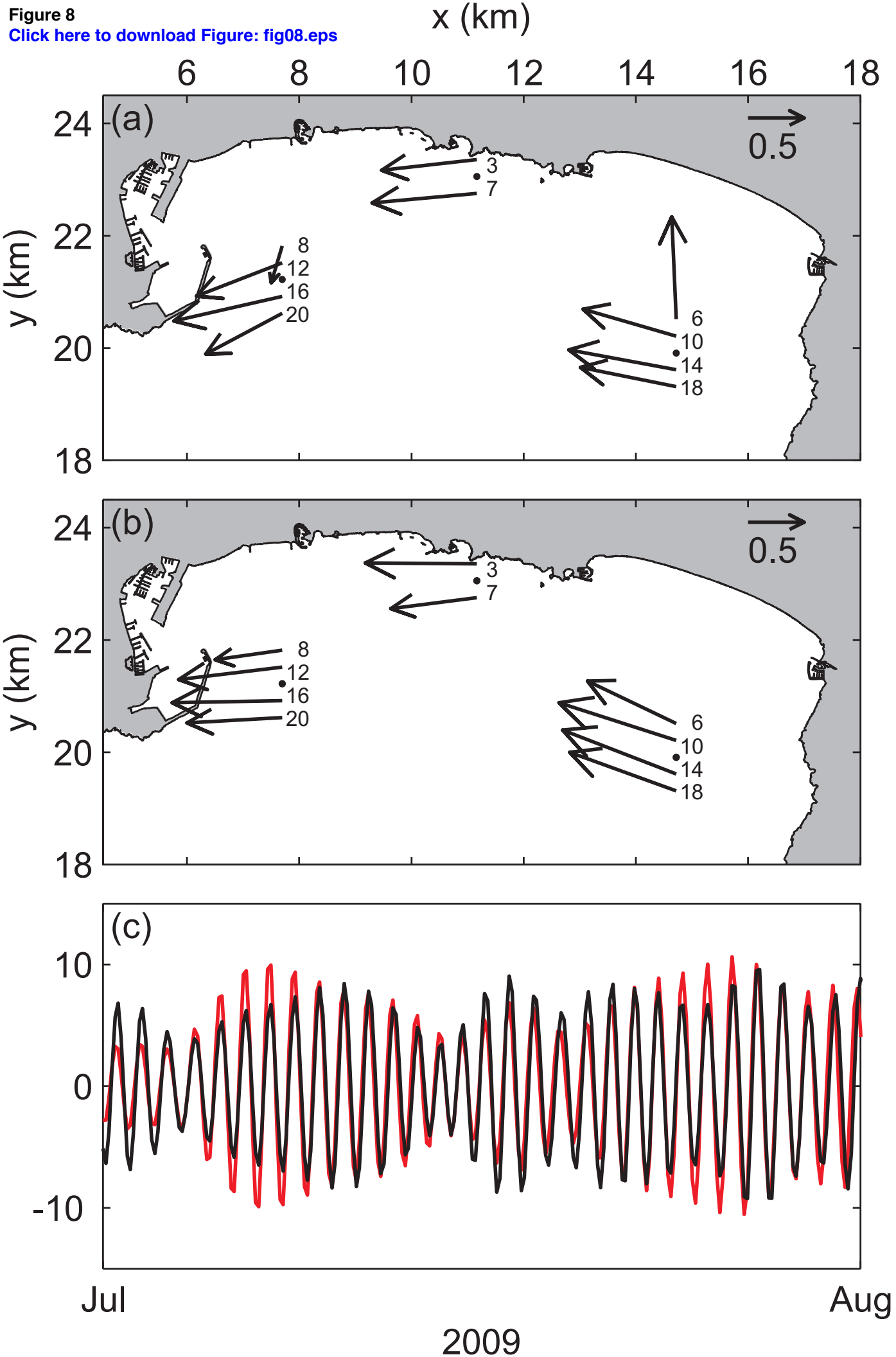

Figure 9
Click here to download Figure: fig09.eps

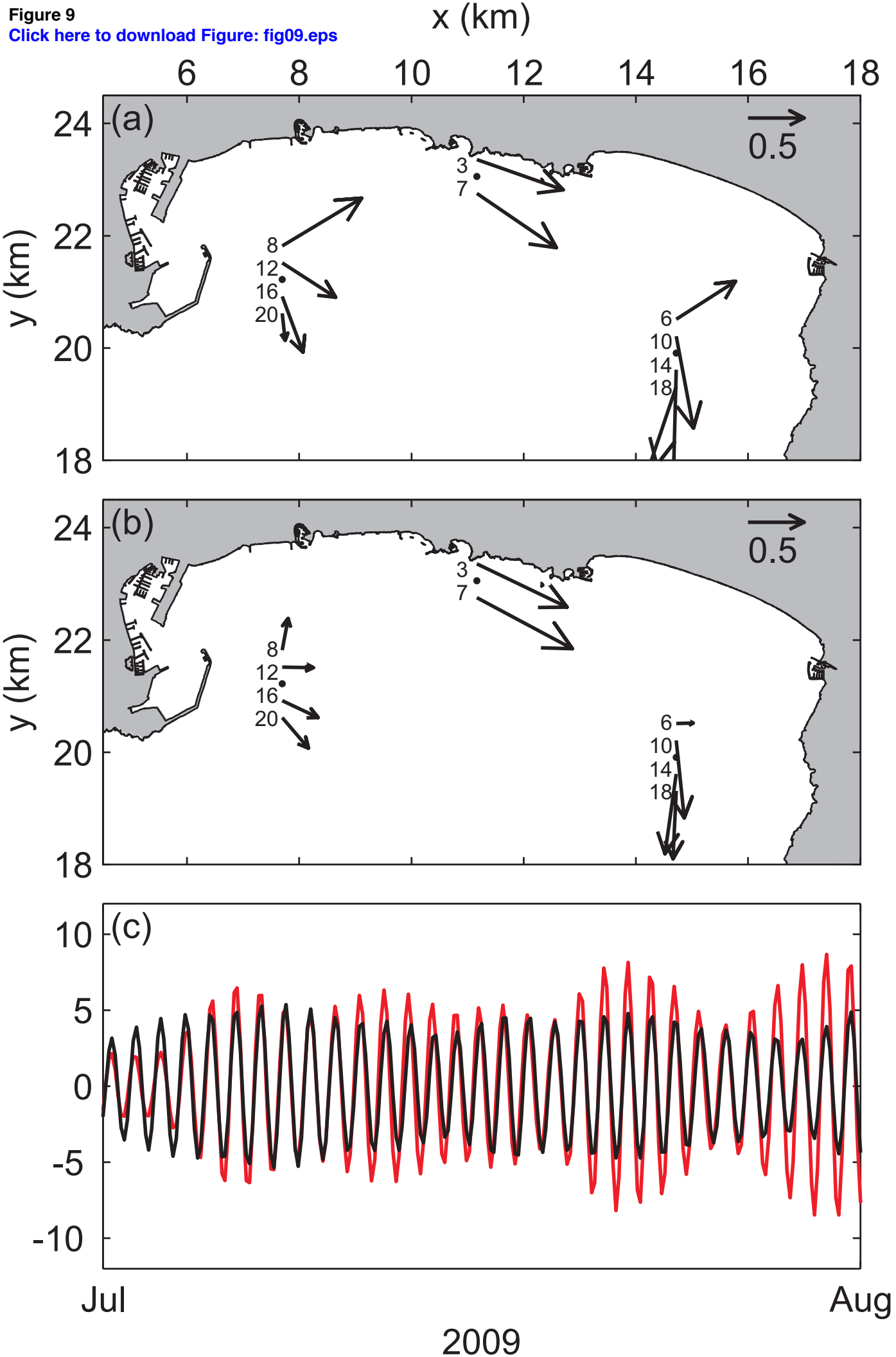

Figure 10
Click here to download Figure: fig10.eps

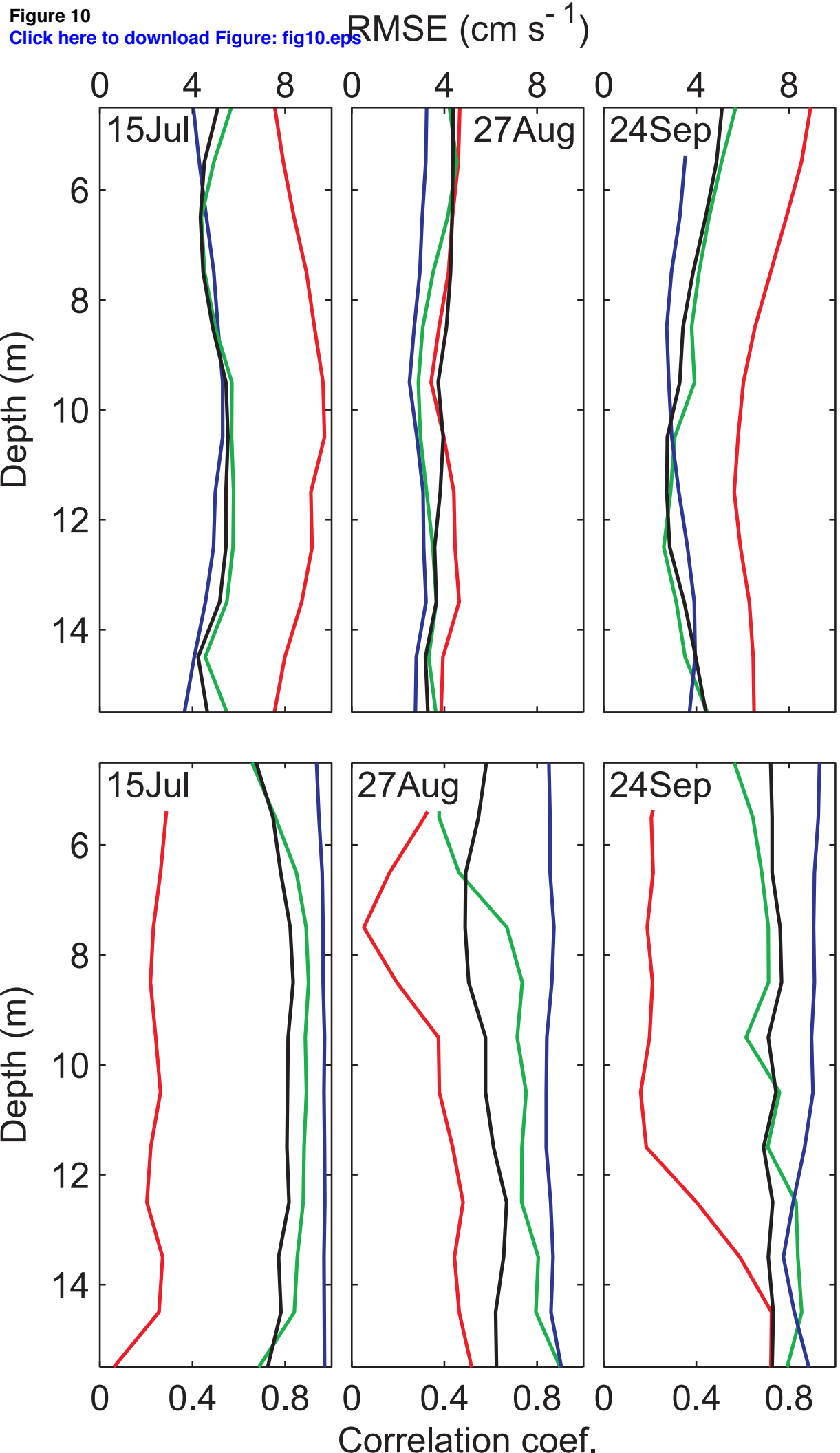

Figure 11
Click here to download Figure: fig11.eps

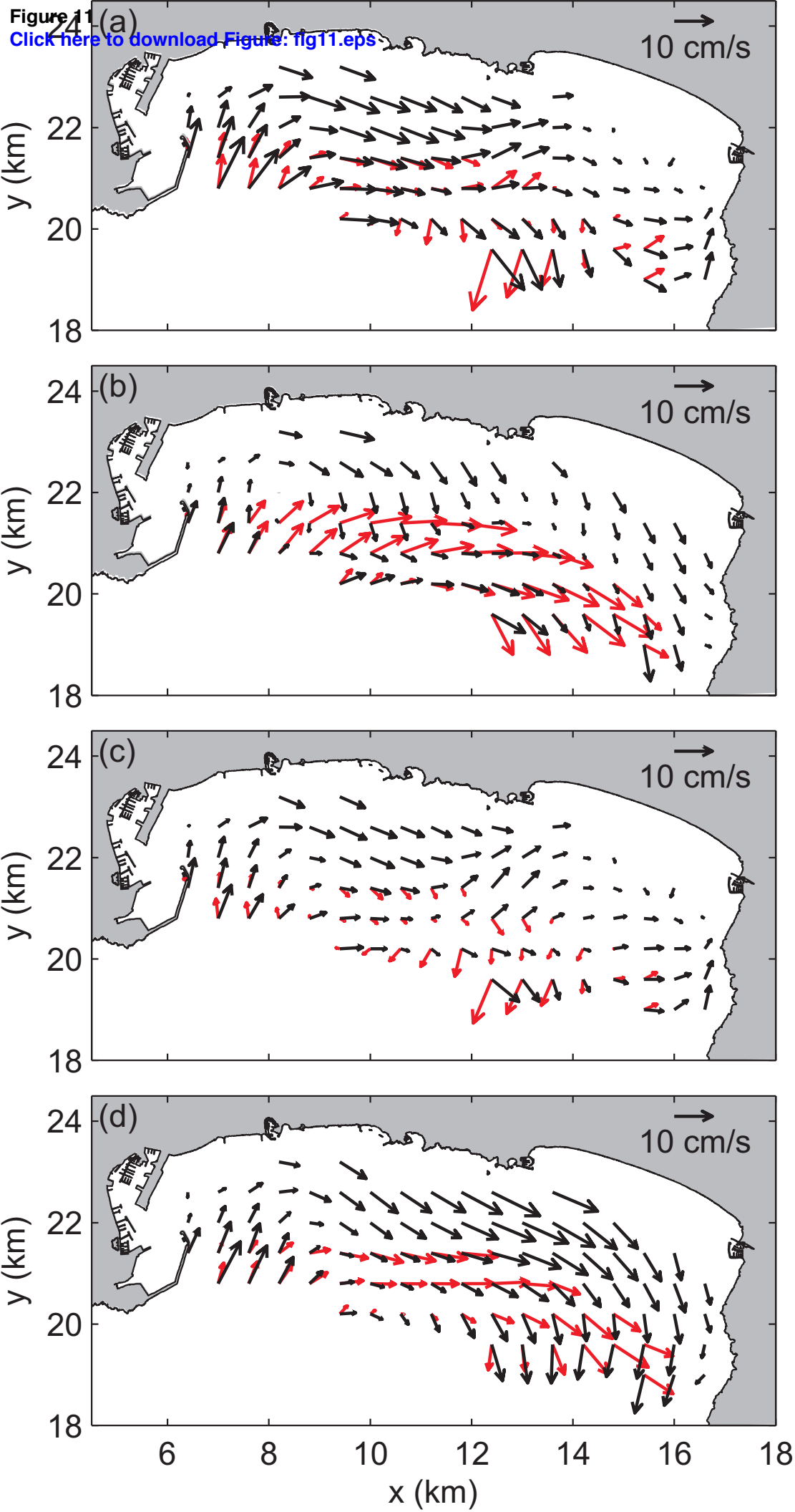

Figure 12
Click here to download Figure: fig12.eps

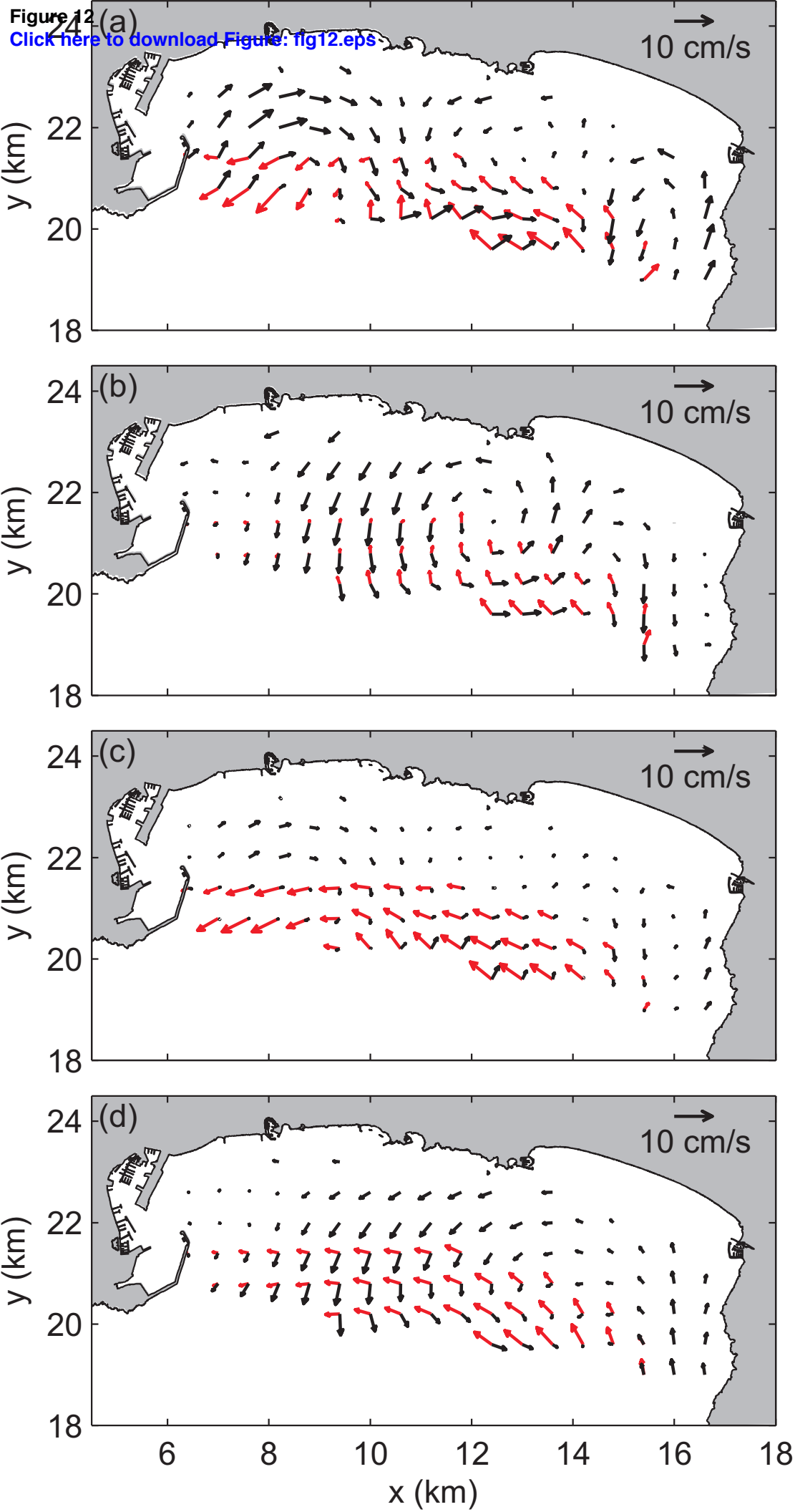

Figure 13
Click here to download Figure: fig13.eps

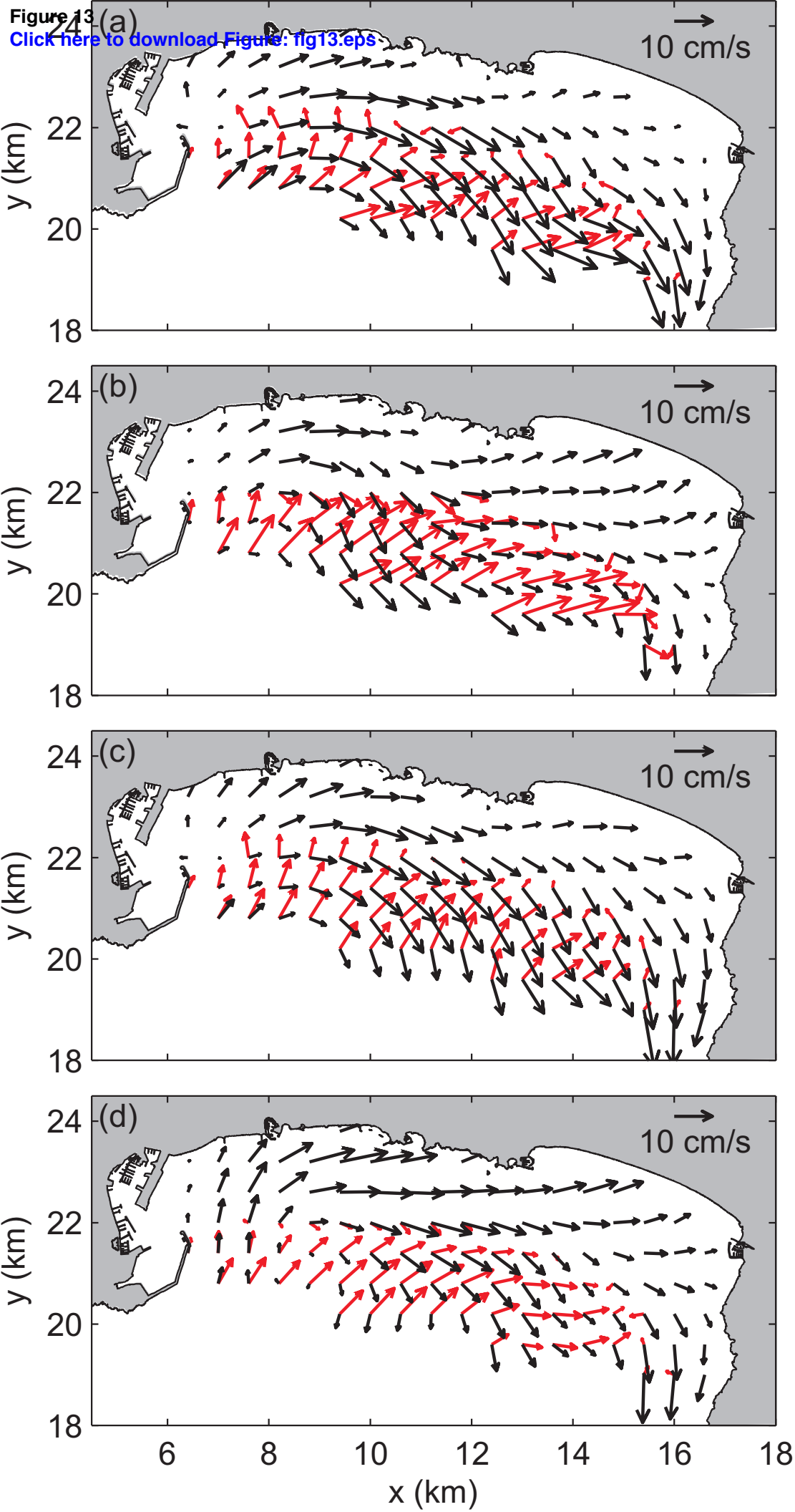

Figure 14
Click here to download Figure: fig14.eps

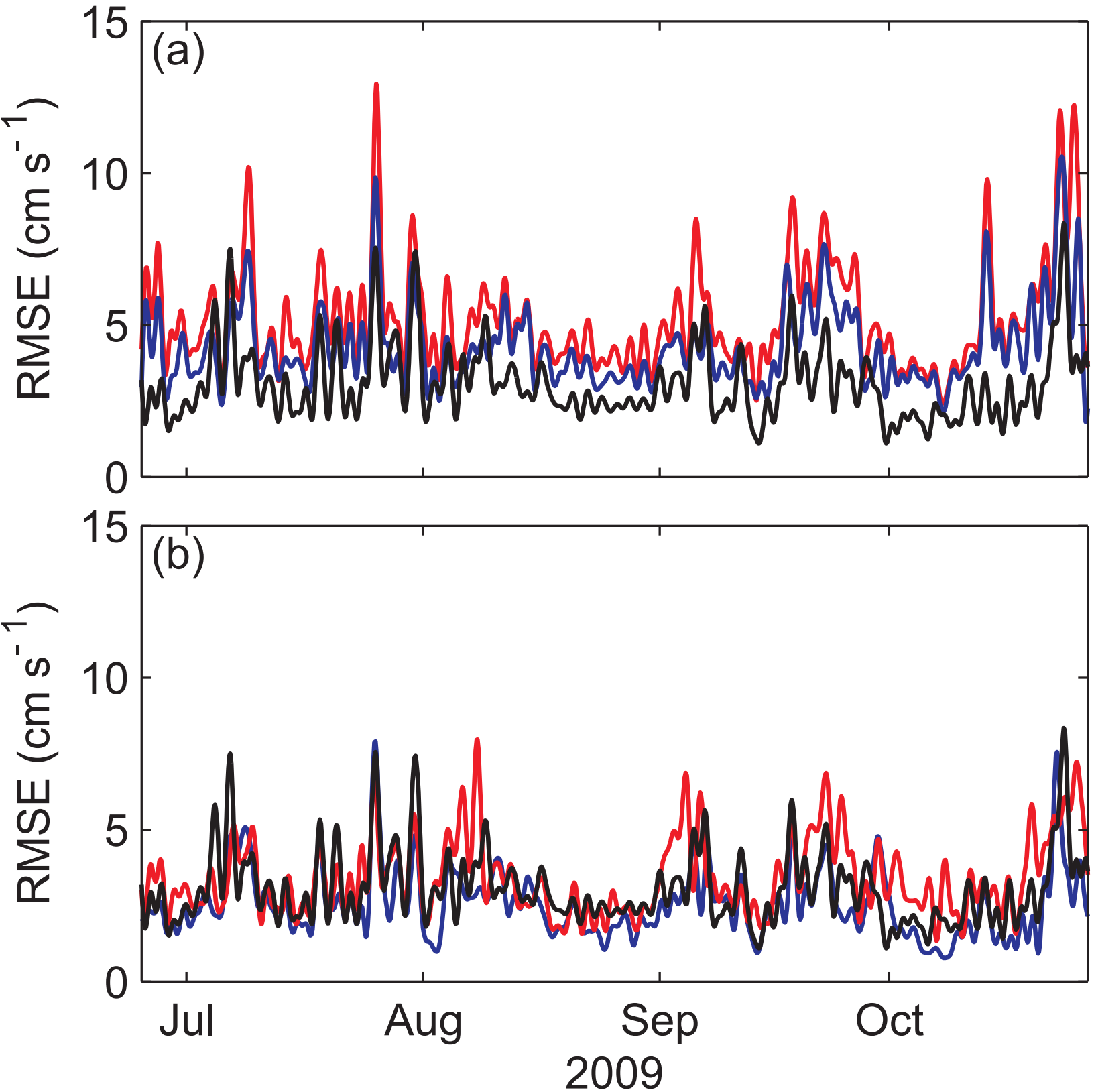

Figure 15
Click here to download Figure: fig15.eps